



Ranjan Pratul (Orcid ID: 0000-0002-2482-3808)

Konstantinou Konstantinos, I (Orcid ID: 0000-0002-6290-9565)

Mapping intrinsic and scattering attenuation in the southern Aegean crust using S-wave envelope inversion and sensitivity kernels derived from perturbation theory

P. Ranjan^{a,b}, K.I. Konstantinou^b

^a Taiwan International Graduate Program- Earth System Science (TIGP-ESS)

^b Department of Earth Sciences, National Central University, Chungli, Taoyuan, Taiwan

Corresponding author: P. Ranjan (pratulanjan@g.ncu.edu.tw)

Key Points:

1. Scattering and intrinsic attenuation from S-envelopes of 104531 crustal events mapped in the southern Aegean using sensitivity kernels
2. High scattering in the Corinth rift, the Santorini-Amorgos zone, and the Gulf of Gökova in agreement with the active faulting.
3. High absorption in Crete and Cyclades linked with metamorphic core complexes while that in Corinth rift associated with fluid activity.

This article has been accepted for publication and undergone full peer review but has not been through the copyediting, typesetting, pagination and proofreading process which may lead to differences between this version and the Version of Record. Please cite this article as doi: 10.1029/2020JB020821

Abstract

We applied sensitivity kernels based on perturbation theory to map the crustal intrinsic and scattering attenuation of S-wave envelopes in the southern Aegean. The southern Aegean crust is under extension due to the rollback of the Nubian plate, which is subducting beneath the Aegean plate. The waveforms of 104531 crustal events (< 40 km) were used to calculate S-wave envelopes in four frequency bands. The S-wave envelopes were modeled using the 3D isotropic solution of the radiative transfer equation with a factor for energy leakage. A two-stage grid search with linear least squares was applied to estimate the attenuation parameters from each S-wave envelope. Then we calculated the 2D scattering and absorption sensitivity kernels for each wave path based on perturbation theory. These kernels and the envelope attenuation parameters were inverted using the Markov Chain Monte Carlo algorithm to obtain maps of intrinsic and scattering attenuation (Q_i^{-1} and Q_{sc}^{-1}). High Q_i^{-1} has thermal origin associated with fluids while high Q_{sc}^{-1} stems from velocity contrasts caused by deformed structure such as faults, folds or fractures. The Corinth rift, the Santorini-Amorgos zone, and the Gulf of Gökova show strong extensional deformation, which may produce high Q_{sc}^{-1} . The deformed oceanic material accreted below the continental crust and fractures generated by large thrust earthquakes likely produce high Q_{sc}^{-1} in Crete. The Corinth rift with its repeated earthquake swarms demonstrate fluid activity, which can explain high Q_i^{-1} . Thermal contrasts generated by metamorphic core complexes is a potential source of Q_i^{-1} in Cyclades and Crete.

1. Introduction

The attenuation of seismic waves is an indicator of the inhomogeneous structure and the anelastic behavior of the Earth. Seismic waves attenuate by two mechanisms: first by the redistribution of energy as it is scattered by inhomogeneous media, known as scattering

attenuation, and second by the conversion of seismic energy to heat, known as intrinsic attenuation (Sato et al., 2012). Crustal estimates of attenuation play a crucial role in monitoring volcanic activities (De Siena et al., 2017; Prudencio et al., 2017) and imaging fracture zones (Gaebler et al., 2019; Napolitano et al., 2020), which enhance our knowledge of the geodynamic processes operating on a larger scale.

Seismic attenuation is quantified by the decay in the amplitude of coda waves with increasing lapse time (time since the origin of the associated event). Aki and Chouet (1975) first observed a nearly exponential decay of coda waves and represented it by the inverse of coda quality factor (Q_c^{-1}). Since then, several studies have measured Q_c^{-1} on a local to regional scale and observed a decreasing trend with the lapse time (Ibáñez et al., 1990; Calvet & Margerin, 2013). Coda waves attenuate by both scattering and absorption (intrinsic) mechanisms. In the domain of early coda (at short lapse times), Q_c^{-1} is the sum of intrinsic attenuation (Q_i^{-1}) and scattering attenuation (Q_{sc}^{-1}). Several studies have inferred Q_{sc}^{-1} in this domain from the delay time of the coda peak (Calvet et al., 2013; Takahashi et al., 2007). However, in the late coda waves, intrinsic attenuation (Q_i^{-1}) is dominant and it is approximated using Q_c^{-1} (Mayor et al., 2016).

The envelopes of seismograms provide joint estimates of Q_{sc}^{-1} and Q_i^{-1} in the region surrounding their wave paths. Separate estimates of Q_{sc}^{-1} and Q_i^{-1} for a half-space model from the envelopes of both early and late coda S-waves were first made using Multiple Lapse Time Window Analysis (MLTWA) (Fehler et al., 1992; Hoshiya, 1993). MLTWA models the integral of an observed S-wave envelope in three time windows after the S-onset to obtain the scattering attenuation (Q_{sc}^{-1}) and the intrinsic attenuation (Q_i^{-1}). The envelope integral in a late coda window normalizes the three S-envelope integrals to cancel the effect of their source energy density and the site amplification. MLTWA is commonly performed in the time domain on the band pass filtered envelopes. Recent studies have also implemented MLTWA in the frequency domain in order to achieve faster computation of envelope integrals (Akinici et al., 2020; Del

Pezzo et al., 2019). As an alternative approach, Eulenfeld & Wegler (2016) inverted the average energy in the early S coda and the envelope in the late S coda to estimate Q_{sc}^{-1} and Q_i^{-1} . The authors used the 3D isotropic solution of the radiative transfer equation to model S-envelopes (Paasschens, 1997). The major advantage of their method over MLTWA was the elimination of the coda normalization step. They fitted the envelopes of all recorded waveforms of an event with a single set of attenuation coefficients and mapped the result using station averaging. However, the waveforms of an event recorded at multiple stations may have encountered different attenuation structure based on the azimuths of the different ray paths. This effect is especially significant in subduction zones where large structural variations exist along different azimuths. Therefore, it is more appropriate to estimate the attenuation parameters based on each S-wave envelope.

The attenuation parameters derived from each S-wave envelope are mapped spatially using sensitivity kernels. Different types of sensitivity kernels exist to map Q_{sc}^{-1} and Q_i^{-1} derived with a half-space model in two dimensions (Del Pezzo et al., 2016; Mayor et al., 2014; Prudencio et al., 2013). The Gaussian distribution based sensitivity kernel proposed by Prudencio et al. (2013) predicts maximum sensitivity at the center of source-station paths. However, the sensitivity kernels derived by both Mayor et al. (2014) and Del Pezzo et al. (2016) predict a maximum at the source and receiver locations. Mayor et al., (2014) used perturbation theory to obtain the scattering and absorption sensitivity kernels for half-space Q^{-1} using the solution of the radiative transfer equation in 2D. Their sensitivity kernels can realistically map the intrinsic and scattering attenuation derived from the S-wave envelopes for different lapse times.

Although seismic attenuation in the southern Aegean has been widely studied by numerous authors (Ventouzi et al., 2018 and references therein), none of these studies have focused on the separation of the intrinsic and scattering attenuation of S-waves. In this work, we combine the S-envelope inversion with the mapping approach based on perturbation theory to obtain the

spatial distribution of scattering and intrinsic attenuation (Q_{sc}^{-1} and Q_i^{-1} respectively) for the southern Aegean. First, we relocate the crustal events (< 40 km) recorded by both permanent and temporary seismic networks and use their waveforms to calculate S-wave envelopes in 1-2, 2-4, 4-8, and 8-16 Hz bands. Then, we invert the S-wave envelopes for the attenuation parameters of each wave-path. Later, the 2D scattering and absorption sensitivity kernels are calculated for each wave path based on perturbation theory. Finally, the attenuation parameters derived from S-wave envelopes, and the sensitivity kernels, are inverted using the Markov Chain Monte Carlo algorithm to obtain the spatial maps of Q_{sc}^{-1} and Q_i^{-1} .

2. Geological and seismotectonic setting

The southern Aegean forms a major part of the Aegean Sea plate that overrides the subducting Nubian lithosphere in the eastern Mediterranean. The Wadati-Benioff zone studies reveal that the dipping angle of the Nubian slab changes from 30° in the fore-arc (up to 100 km depth) to 45° in the back-arc (Papazachos et al., 2000). The convergence between the Eurasian and the Aegean Sea plate (~ 35 mm/yr), which is faster than the one between the Eurasian and the Nubian plate (~ 9 mm/yr) (Figure 1), is associated with the Nubian slab rollback as well as the westward escape of the Anatolian plate bounded by the North and East Anatolian faults (Argus et al., 2011; Reilinger et al., 2006). These driving forces have caused extension in the Aegean crust and resulted in the formation of the Aegean Sea during the Oligocene-Miocene. The extension also induced the SW motion of the volcanic arc, whose current position is at the southern boundary of the island group of Cyclades. The Cyclades exhibit outcrops of metamorphic core complexes (MCCs) also exhumed because of the extension in the Aegean crust (Tirel et al., 2008). The rates of extension are the fastest across the Gulf of Corinth (> 10 mm/yr), where the occurrence of multiple earthquake swarms confirms the existence of fluids (Avallone et al., 2004; Kapetanidis et al., 2015). The Corinth rift separates the Hellenides mountain belt into the north and south belt. The southern Hellenides spanning Peloponnese,

were formed by the thrusting of sedimentary rocks as well as the accretion of crustal slices from the subducting slab to the Aegean crust (Burchfiel et al., 2018). The accretion of subducting slab material to the overriding plate is in progress all along the fore-arc, including the island of Crete and it is cited as one of the mechanisms, which causes crustal uplift in Crete (Ott et al., 2019). As a result of these processes, the crustal thickness across the southern Aegean varies considerably with an average thickness in the range of 23-27 km across Crete island, the Sea of Crete and the Cyclades while it is between 32 to 43 km below Peloponnese (Sodoudi et al., 2006).

The azimuths of the maximum and minimum stress axes reveal a variable style of faulting across the southern Aegean (Kapetanidis & Kassaras, 2019; Konstantinou et al., 2017). NE-SW right-lateral strike-slip faults dominate in a high seismicity zone at the western termination of the Hellenic arc known as the Kefalonia Transform Zone (Kokinou et al., 2006). The seismicity across most of Peloponnese and the Gulf of Corinth occurs on E-W normal faults (Shaw & Jackson, 2010). NNE-SSW and WNW-ESE normal faults accommodate arc-parallel and arc-normal extension respectively on the island of Crete (Caputo et al., 2010). The westernmost margin of Crete also exhibits seismicity along NW-SE thrust faults that are likely responsible for the 365 AD (M_w 8.2) earthquake (Shaw et al., 2008). Along the eastern margin including the Gulf of Gökova, events occur on E-W to ENE-WSW normal faults (Andinisari et al., 2019). Clusters of microseismicity along the Hellenic arc with high waveform similarity suggest that the fluids released during slab dehydration migrate along active faults nearing failure (Ruscic et al., 2019). Along the volcanic arc and in the back-arc, small magnitude volcano-tectonic earthquakes occur near the land-based and submarine volcanoes (Konstantinou et al., 2013).

3. Data and envelope calculation

The data used in this work comprises of 104531 events ($M_L < 3.5$; depth ≤ 40 km) recorded by the seismic stations of three different networks:

1) The Hellenic Unified Seismic Network (HUSN), a nationwide network of 150 broadband stations that includes the following seismic networks operated by: the Geodynamic Institute, of the National Observatory of Athens (NOA) - HL, the Geophysical Department of the Aristotle University of Thessaloniki (AUTH) - HT, the Department of Geophysics and Geothermics of the National and Kapodistrian University of Athens (NKUA) - HA, and the Geological Department, of the University of Patras (UPAT) - HT (<http://www.gein.noa.gr/en/networks/husn>);

2) EGELADOS (Exploring the GEodynamics of subducted Lithosphere using an Amphibian Deployment Of Seismographs), a temporary seismic network that operated from late 2005 to early 2007, consisting of 56 broadband stations across the southern Aegean (Friederich & Meier, 2005), seven short-period stations from the GEOFON network and one broadband station from the MEDNET (MEDiterranean NETwork) (Boschi et al., 1991);

3) CYCNET (CYClades seismic NETwork), temporary network of 23 broadband stations in the Cyclades (Meier et al., 2004) that operated from autumn 2002 to early 2004.

All events were relocated using a minimum 1D velocity model for the southern Aegean (Brüstle et al., 2012) with NonLinLoc (Lomax et al., 2000) and only events with hypocentral depths < 40 km and location errors less than 5 km in the vertical and horizontal directions were selected (Figure S1). The events with $M_w > 3.5$ recorded by EGELADOS and CYCNET stations were removed based on the Global Centroid Moment Tensor (GCMT) and the European-Mediterranean Regional Centroid-Moment Tensors (RCMT) catalogues. The NOA catalogue was used to remove the events with $M_L > 3.5$ from the relocated HUSN events. We chose this

upper bound on the magnitude of events so that we can approximate their source-time functions as impulses. The three component seismograms from the final events were filtered in 1-2, 2-4, 4-8, and 8-16 Hz frequency bands. The final 104531 events and the station sites are shown in Figure 2 and their ray coverage for all frequency bands is shown in Figure 3.

We calculated the mean-square envelopes of the bandpass-filtered three component velocity seismograms by taking the squared mean of each component and its Hilbert transform, and summing it over the three components. This was multiplied by the average density of the continental crust (2830 kg/m^3) and divided by the gap between corner frequencies of the filter used as well as by the free surface correction factor (see Emoto et al., 2010) to obtain the observed energy envelope in each frequency band (Eulenfeld & Wegler, 2016; Sato et al., 2012). After that, we measured the noise level of the envelope as the minimum average amplitude in multiple 5 s windows before the P arrival and using this noise level, we calculated the signal to noise ratio (SNR) of the envelope. Each envelope was cut from 1 s before the S-onset up until the SNR dropped below 3, or up to a maximum lapse time of 100 s. The envelope was also cut short if a sudden jump in the SNR was observed in the coda, which is often due to interference with other seismic signals or noise. We also smoothed the S-envelopes by convolving them with a Bartlett window. Envelopes in all frequency bands were smoothed over equal number of cycles so that they could retain the features characteristic of their frequency band, hence smaller length Bartlett windows were used for the envelopes in higher frequency bands. We tested different values for the number of cycles, however, we did not observe any significant difference in the results (see section 5). Therefore, we finally used 7.2 s, 3.6 s, 1.8 s, and 0.9 s length Bartlett windows for smoothing the envelopes in 1-2 Hz, 2-4 Hz, 4-8 Hz, and 8-16 Hz bands respectively as it showed lower error on average in the fitting of envelopes.

4. Methodology

4.1 Forward Model

The S-envelope of an event waveform in a particular frequency band is given by (modified from Eulenfeld & Wegler, 2016)

$$E_{calc}(r, t, f) = W(f) \times R(f) \times G(r, t, g^*(f)) \times e^{-b(f)t} \times e^{-b_{lk}(g^*(f), H)t} \dots \dots \dots (1)$$

where W is the spectral source energy, R is the site amplification term, $G(r, t, g^*)$ is the Green's function representing the response of an impulsive source, g^* is the scattering coefficient, b is the intrinsic attenuation coefficient, b_{lk} is the leakage coefficient, H is the Moho depth below the epicenter of the event, r is the hypocentral distance of the station from the source, t is the time since event origin and f represents the frequency band.

The leakage coefficient (b_{lk}) accounts for the leakage of seismic energy into the mantle from crustal events. This energy leakage results in the decreasing trend of Q_c^{-1} with the depth of the events used (Badi et al., 2009; Ibañez et al., 1990). For short epicentral distances, the effect of energy leakage is significant even at small lapse-times while for large epicentral distances, the energy leakage is significant only at large lapse times (Margerin et al., 1998). As the intrinsic attenuation is dominant in late coda waves, the inverse of coda quality factor (Q_c^{-1}) measured as the slope of the decaying late coda energy can represent the inverse of intrinsic quality factor (Q_i^{-1}). The Q_c^{-1} is equal to the sum of Q_i^{-1} and Q_l^{-1} (inverse of leakage quality factor) in late coda waves. Margerin (2017) derived an equation to calculate Q_l^{-1} :

$$Q_l^{-1} = \frac{c}{\omega \times l^* \times (1-g) \times \tau_l(H/l^*)} \dots \dots \dots (2)$$

where c is the medium velocity, ω is the angular frequency, l^* is the mean free path which is the inverse of scattering coefficient (g^*), g is the anisotropy factor, and τ_l is the mean free time which is a function of Moho depth (H) normalized by l^* . τ_l can be approximated using the plot

of τ_l vs. H/l^* for rough surfaces provided in Margerin (2017) and g is set to 0 for isotropic scattering. Q_l^{-1} can provide leakage coefficient (b_{lk}) as:

$$b_{lk} = Q_l^{-1} \times \omega \dots \dots \dots (3)$$

The Moho depth for the southern Aegean is highly variable because of the complex tectonics of this region. Receiver function analysis in this region only provides local average estimates of Moho depth (Soudoudi et al., 2006). We interpolated these local estimates using Delaunay triangulation method and calculated the parameter H for each event based on their spatial location, for use in equation (2). We included the leakage coefficient (b_{lk}) in the equation used by Eulenfeld & Wegler (2016) by simply replacing b with the sum of b and b_{lk} , which is equivalent to replacing Q_l^{-1} by the sum of Q_l^{-1} and Q_l^{-1} .

The Green's function used in equation (1) should approximate the overall shape of the observed envelopes. We use the isotropic solution of the radiative transfer equation in 3D (Paasschens, 1997) as the Green's function. We divide each S-envelope into 2 parts: the early-S window and the S-coda window. The early-S window starts at the S-onset and ends at twice the S-envelope peak location. We compare the mean of the energy in the early-S window. We observed that the fitting between the observed and the calculated envelopes improves by comparing two means in the early-S window: one for the full early-S window assigned to the time of S-envelope peak and the other for the half early-S window assigned to half of the time of S-envelope peak. The S-coda window continues from the end of the early-S window to the end of the S-envelope. We used envelopes in the inversion only if the S-coda window length was > 8 s, since this condition ensured sufficient length for envelope fitting.

Taking the logarithm of equation (3), replacing E_{calc} with the observed S-envelope (E_{obs}) and rearranging we get

$$\log \left(\frac{E_{obs}(r,t,f)}{G(r,t,g^*(f)) \times \exp(-b_{lk} \times t)} \right) = (-b(f) \times t) + \log(W(f) \times R(f)) \dots \dots \dots (4)$$

The above equation is linear in time and can be solved for b using a fixed value of g^* by applying linear inversion techniques (see section 4.2). Once the values of b and g^* are known, the theoretical envelope (E_{calc}) can be calculated using equation (1). The error term (ε) to estimate the goodness of envelope fitting is given as

$$\varepsilon = \left(\log \left(\frac{E_{obs}(r,t_1,f)}{E_{calc}(r,t_1,f)} \right) \right)^2 \times \omega_1 + \left(\log \left(\frac{E_{obs}(r,t_2,f)}{E_{calc}(r,t_2,f)} \right) \right)^2 \times \omega_2 + \sum_{i=3}^{N_t} \left(\log \left(\frac{E_{obs}(r,t_i,f)}{E_{calc}(r,t_i,f)} \right) \right)^2 \dots \dots \dots$$

(5)

where t_1 represents the time of the half of the S-envelope peak, ω_1 is a weight equal to the half-length of the early-S window, t_2 represents the time of the S-envelope peak, ω_2 is a weight equal to the length of the early-S window and N_t is the length of the S-envelope.

4.2 Inversion method

We invert for g^* and b using a two-stage grid search combined with linear least squares algorithm for each source-station pair in each frequency band. In the first stage, a search set for g^* is defined with 50 logarithmically spaced points between 10^{-4} and 10^1 km^{-1} . Then, $G(r, t, g^*(f))$ and b_{lk} are estimated for each g^* in the set, and b is calculated for each case using the linear least-square inverse of equation (4) obtained with the help of QR factorization. The g^* that gives the minimum value of the error term (ε) is used thereafter as g_{min}^1 . In the second stage, we define a second search set with 50 logarithmically spaced points between the two values preceding and succeeding g_{min}^1 in the first set. We calculate G , b_{lk} , b , and ε for each g^* in the second search set in a similar manner as the first stage. The scattering coefficient of the wave path is determined as the g^* from the second search set, that minimizes the second stage error term (ε). Then, the corresponding b calculated using equation (4) is the intrinsic coefficient of the particular path. We repeat the same process for all the source-station pairs in all frequency bands (Figure 4). Our algorithm has some similarities with the golden section

search used by Eulenfeld and Wegler (2016), as both approaches optimize unimodal functions and have a trade-off between performance and accuracy. We speed up the inversion by employing matrix algebra techniques to estimate G for the two search arrays of g^* . The errors in estimating g^* are within a fixed logarithm around its true value. This feature is desirable, as we finally compare the spatial distribution of the logarithm of intrinsic and scattering attenuation, not the values in linear scale. It took approximately 30 hours to calculate all the intrinsic and scattering coefficients in all frequency bands from the raw waveforms on a fourth generation Intel i7 machine with 26 gigabytes of RAM. Using the inverted g^* and b , the intrinsic and scattering Q^{-1} were estimated as (Carcolé & Sato, 2010)

$$Q_{sc}^{-1} = \frac{g^* v_{avg}}{2\pi f}, \quad Q_i^{-1} = \frac{b}{2\pi f} \dots\dots\dots (6)$$

v_{avg} represents the average crustal velocity for each station and was measured using all the S-onsets for that station. The Green's functions were also estimated using v_{avg} for the station in a source-station pair. We observed that v_{avg} values for all the stations were relatively similar, varying between 3.1 and 3.5 km/s. Using Q_{sc}^{-1} and Q_i^{-1} , the seismic albedo (B_o) can be also calculated as

$$B_o = \frac{Q_{sc}^{-1}}{Q_{sc}^{-1} + Q_i^{-1}} \times 100 \% \dots\dots\dots (7)$$

B_o measures the percentage scattering attenuation out of the total S-wave attenuation. High B_o indicates high scattering attenuation as compared to intrinsic attenuation. Similarly, low B_o indicates high intrinsic attenuation and low scattering attenuation. The average percentage errors in the fitting of the S-envelopes for all frequency bands are shown in Figure S2. Both the early-S window and the whole S-envelope show the most broadened distribution in 1-2 Hz band. This is probably because of the longer period of signal oscillations in this band.

4.3 Mapping method

Recently several sensitivity kernels have been proposed for a realistic spatial mapping of Q^{-1} . Theoretical kernels derived using perturbation theory with mean medium attenuation coefficient show that the maximum sensitivity points lie at the source and receiver locations (Mayor et al., 2014; 2016). Kernels derived using Monte-Carlo simulations of energy particles seem to follow a multi-modal distribution for a lapse time of 15 s (Del Pezzo et al., 2016; Ibáñez et al., 2019; Prudencio et al., 2018) and approximate the absorption kernels derived using perturbation theory. However, the kernels based on Monte-Carlo simulations were empirically derived for a lapse time of 15 s and therefore we do not know whether the approximation will hold for larger lapse times. The Gaussian mapping approach is the simplest to implement, however, it assumes that the maximum sensitivity point lies at the center of source-station paths (Prudencio et al., 2013). In this study, we calculate the absorption and scattering sensitivity kernels for each source-station path following Mayor et al. (2014) using the scattering mean free path (inverse of scattering coefficient) and the lapse times obtained from the inversion. An undesirable feature of these sensitivity kernels is that they predict a singularity at the source and receiver positions. However, using a large bin size, we only have to evaluate the sensitivity kernels near the source and receiver locations where their values are finite. This helps smooth the sensitivity kernels, and hence we divide the southern Aegean into $0.20^\circ \times 0.20^\circ$ bins. The computer memory required to create and invert such kernels was also a limiting factor on the size of the bins used for mapping. The intrinsic attenuation and the scattering attenuation for each bin relates to the intrinsic attenuation and the scattering attenuation from each ray path as follows:

$$(Q_i^{-1})_n = \sum_n K_a^{nm} \times (Q_i^{-1})_m \dots \dots \dots (8)$$

$$(Q_{sc}^{-1})_n = \sum_n K_{sc}^{nm} \times (Q_{sc}^{-1})_m \dots \dots \dots (9)$$

where n is the ray-path number, m is the bin number, K_{sc} is the normalized and absolute valued scattering sensitivity kernel, K_a is the normalized and absolute valued absorption sensitivity

kernel, $(Q_{sc}^{-1})_m$ is the scattering attenuation for m^{th} bin (similarly for Q_i^{-1}), and $(Q_{sc}^{-1})_n$ is the scattering attenuation for n^{th} envelope (similarly for Q_i^{-1}). Studies have shown previously the dependence of Q_c^{-1} on lapse time (Calvet & Margerin, 2013) and as Q_c^{-1} is mainly composed of Q_i^{-1} , we observe this decay for Q_i^{-1} as well. This decay occurs because at longer lapse times seismic waves sample larger regions, effectively reducing the Q_i^{-1} measured from the seismic envelope. To account for this effect, the sensitivity kernels discussed above increase (decrease) in size for large (small) lapse times. Also, the spatial variation of kernel amplitudes changes based on the lapse time. Therefore, when we invert for the spatial Q_i^{-1} (discussed below) with equation (8) as the forward model, the lapse time effect is automatically taken into account by the sensitivity kernels. We note that Mayor et al. (2016) used an additional factor of the inverse of lapse time in equation (8) because they applied coda normalization to the sensitivity kernels, which aims to remove the effect of the source energy and the site amplification on estimated Q_c^{-1} and account for the decay of coda intensity with lapse time. As we already removed the source energy and the site amplification terms during inversion (equation 4), we normalize the absolute valued sensitivity kernels using their sum and therefore, this additional factor is not required.

We invert the equations (8) and (9) for Q_{sc}^{-1} and Q_i^{-1} of each bin by applying the Markov Chain Monte Carlo method using Metropolis-Hastings algorithm (Chib & Greenberg, 1995). We only used ray paths having errors less than the mean logarithm of percentage error in the early-S window, for each frequency band (Figure S2). In addition, unrealistic values for g^* and b obtained from envelope inversion were also removed after manual inspection of envelope fitting such that $g^* \in (10^{-4}, 0.2) \text{ km}^{-1}$ and $b \in (10^{-3}, 0.2) \text{ s}^{-1}$. Apart from that, we also removed ray paths with epicentral distances less than the bin spacing (0.20°). Finally, we used 58330 S-envelopes in 1-2 Hz, 203560 in 2-4 Hz, 221748 in 4-8 Hz, and 233862 in 8-16 Hz band. At the start of the inversion, a scalar Q^{-1} (Q_{sc}^{-1} , Q_i^{-1}) is assigned to all the bins which minimizes the

difference between L.H.S. and R.H.S. in equations (8) and (9) by searching from a set of logarithmically spaced values in the range 10^{-5} to 10^0 . A random error of 10 percent is also added to all the bins to make the bin values different from each other. Then, iteratively the Q^{-1} value in a randomly selected bin is perturbed by choosing a random number from a Gaussian distribution centered at the value of the bin. After that, the theoretical Q^{-1} of each ray path is calculated using equations (8) and (9) with the help of perturbed Q^{-1} model. A likelihood function compares the difference between the observed ray Q^{-1} and the modeled ray Q^{-1} . The likelihood function for Q_i^{-1} is formulated as:

$$\mathcal{L} = \exp \left(- \sum_n \frac{((Q_i^{-1})_n^{mod} - (Q_i^{-1})_n^{obs})^2}{\sigma_i^2} - N_{ray} \times \sum_m \left(\nabla^2 (\log((Q_i^{-1})_m^{mod})) \right)^2 \right) \dots \dots \dots \quad (10)$$

where subscripts m and n denote bin numbers and ray path number respectively, superscripts mod and obs denote modeled and observed parameters respectively, Q_i^{-1} is the intrinsic attenuation, σ_i is the standard error of intrinsic attenuation parameter, N_{ray} is the total number of ray paths, and ∇^2 is the 2D Laplacian operator for smoothing. In case of scattering attenuation, Q_i^{-1} was replaced by Q_{sc}^{-1} and σ_i was replaced by σ_{sc} in the above formula. We take the ratio of the likelihood function values for two consecutive perturbed models and compare it to a uniform random number between zero and one. If this ratio exceeds the random number or one then the perturbed bin value is accepted, otherwise rejected. The algorithm was run for 3,000,000 iterations for Q_i^{-1} and 5,000,000 iterations for Q_{sc}^{-1} and the models in the final 100,000 iterations were averaged. The parameters related to MCMC method are provided in Table S1 and the convergence is shown in Figure S3 of the supporting information. The map of Q_{sc}^{-1} and Q_i^{-1} using Gaussian kernels is shown in Figure S4 for reference. The seismic albedo for each bin was calculated using equation (7). The Q_{sc}^{-1} , Q_i^{-1} , and B_o datasets were all smoothed using the Generic Mapping Tools (GMT) (Wessel et al., 2019) *blockmean* command (with 20

arc minutes spacing) and *surface* command (with tolerance of 0.25 and spacing of 0.01°). *Blockmean* averages the data in each block using L2 norm and *surface* interpolates a grid using continuous curvature splines (see GMT documentation at <http://gmt.soest.hawaii.edu/doc/latest/index.html> for more info). These commands have been used with a tolerance of 0.25 as recommended in the GMT documentation to apply spatial smoothing to our results. For comparison, Carcolé & Sato (2010) used a more strict tolerance of 1 with the *surface* command as they worked with the higher density Hi-net seismic network.

5. Results

The results for $\log_{10}(Q_{sc}^{-1})$, $\log_{10}(Q_i^{-1})$ and the seismic albedo are shown in Figures 5, 6, and 7 respectively. High scattering attenuation and high intrinsic attenuation regions are identified in the Cyclades, the Gulf of Corinth and NW Peloponnese, the Kefalonia Transform Zone, Crete, and the Gulf of Gökova across the four frequency bands. High scattering regions are similar in all frequency bands while the regions with high intrinsic attenuation change with the frequency band. The results show consistently high intrinsic attenuation as well as scattering attenuation in the Gulf of Corinth in all frequency bands. This region also shows higher scattering attenuation than intrinsic attenuation in all frequency bands. The Cyclades displays medium to high scattering attenuation from low to high frequency bands while strong intrinsic attenuation up to 2-4 Hz band. The Gulf of Gökova shows strong scattering attenuation in 1-2 Hz and 8-16 Hz bands while high to moderately high intrinsic attenuation from low to high frequency bands. Crete indicates strong scattering attenuation in all frequency bands while moderately high intrinsic attenuation in 1-2 Hz and 4-8 Hz bands. In the Gulf of Gökova, scattering attenuation is dominant up to 4-8 Hz while in Crete scattering attenuation is dominant in all frequency bands. Even though Kefalonia Transform Zone (KFZ) is at the western edge of our network and rays sample this region from only one side, it seems to exhibit high intrinsic and

high scattering attenuation in all frequency bands, similar to the Gulf of Corinth. KFZ also shows relatively higher scattering than intrinsic attenuation up to 4-8 Hz band. Among the volcanic centers (Figure 1), the Santorini-Kolumbo group shows the highest scattering attenuation in all frequency bands. The Methana-Sousaki volcanic group shows the highest intrinsic attenuation up to 2-4 Hz band while the Kos-Yali-Nisyros group shows the highest intrinsic attenuation in 4-8 Hz and 8-16 Hz band. Milos does not show high scattering attenuation and it only shows high intrinsic attenuation in 1-2 Hz band. Overall, scattering attenuation dominates in the low frequency band (1-2 Hz, and 2-4 Hz) while intrinsic attenuation dominates in the high frequency bands (4-8 Hz, and 8-16 Hz) (Figure 7). The southern Aegean displays a decreasing trend for both scattering attenuation and intrinsic attenuation with increasing frequency band. We also show the maps of $\log_{10}(Q_{sc}^{-1})$ and $\log_{10}(Q_i^{-1})$ for different degree of smoothing of S-envelopes in Figures S5 and S6 of the supporting information respectively. From these maps, it is clear that the changes in the degree of smoothing has minimal effect on the results as long as the envelopes showing high logarithmic percentage error in the early-S window are rejected (Figure S2).

6. Checkerboard Tests

A checkerboard test determines the spatial resolution of the source-station paths. To perform the test, we divided the southern Aegean into $100 \text{ km} \times 100 \text{ km}$ rectangular cells that comprise of bins having a node spacing of $0.20^\circ \times 0.20^\circ$. We assigned high anomalies ($Q_{sc}^{-1} = 5 \times 10^{-2}$ and $Q_i^{-1} = 10^{-2}$) and low anomalies ($Q_{sc}^{-1} = 10^{-2}$ and $Q_i^{-1} = 10^{-3}$) in alternate cells to form the checkerboard pattern (Figure S7 (a), S8 (a)). Then, we calculated the initial Q_{sc}^{-1} of each wave-path as the inner product of the scattering sensitivity kernel (calculated using observed mean free paths and lapse times) with the Q_{sc}^{-1} in all the bins. Similarly, we obtained the initial Q_i^{-1} of each wave-path and used equation (6) to calculate its g^* and b values. The theoretical

envelopes for each wave path were calculated using equation (1) and perturbed by adding 10 percent random noise. We solved the perturbed envelopes using equations (4) to (6) to obtain the inverted Q_{sc}^{-1} and Q_I^{-1} of the wave paths. Then, the bin Q_{sc}^{-1} and Q_I^{-1} were calculated using the MCMC approach with the help of equations (8) to (10). The inverted checkerboard maps were generated using GMT in the same way as the original Q_{sc}^{-1} and Q_I^{-1} maps. This process was repeated in all four frequency bands (Figure S7 (b-e), S8 (b-e)).

We recovered to a good extent the checkerboard pattern across most of the southern Aegean up to 2-4 Hz band for both Q_{sc}^{-1} and Q_I^{-1} . In the 4-8 Hz and 8-16 Hz band, the Q_{sc}^{-1} anomalies appear more smoothed out in the Sea of Crete and in the portion of the central Aegean Sea, north of the Cyclades. As we use a fixed checkerboard of Q_{sc}^{-1} and Q_I^{-1} in all frequency bands, the g^* calculated in high frequency bands (using equation 6) would be unrealistically high in some cases and there may be a large error in estimating this g^* through the inversion. This leads to the rejection of many data points and lower resolution, especially in areas with low station density like the Sea of Crete and the central Aegean Sea. Therefore, we will not discuss any further the results regarding the portion of the central Aegean Sea that overlaps our study area and the Sea of Crete.

7. Discussion

Intrinsic attenuation refers to various mechanisms that convert seismic energy to heat through friction, viscosity, and thermal relaxation processes (Sato et al., 2012). These processes cause significant attenuation at high temperatures and in the presence of fluids, therefore seismic waves undergo high intrinsic attenuation when they interact with hot ductile rocks and fluid filled pores/cracks. Scattering attenuation refers to the mechanisms that redistribute seismic energy in the medium without converting it to other forms. Density or velocity perturbations at small scales generated by inhomogeneous structures such as faults, folds or fractures scatter

seismic waves in different frequency bands. The amount of scattering attenuation, therefore, depends on the degree of inhomogeneity in the medium. Our scattering and absorption maps mark four main regions characterized by strong anomalies: the Corinth rift, the Santorini-Amorgos zone, Crete and the Gulf of Gökova. Therefore, we discuss the results by interpreting the scattering and intrinsic attenuation in each of these regions through comparison with the geology, seismotectonics, and previous studies in the southern Aegean.

In the Gulf of Corinth, we observe high Q_i^{-1} and high Q_{sc}^{-1} in all frequency bands. High Q_{sc}^{-1} regions are closely associated with a shallow (5-15 km) north-dipping zone of continuous earthquake activity identified by seismicity studies in this area (Mesimeri & Karakostas, 2018 and references therein). This zone forms the root of the shallow faults that have normal and strike-slip components as imaged in seismic sections (Beckers et al., 2015). Some of these faults, like the ones along the northern Peloponnese coast, evidence themselves as low S-velocity zones in ambient noise tomography (Giannopoulos et al., 2017). High Q_i^{-1} regions overlap with the epicenters of several earthquake swarms with high slip rate, short event duration, and fluid related origin (Kapetanidis et al., 2015; Pacchiani & Lyon-Caen 2010). Recent body wave tomography at the western Gulf of Corinth reveals high V_p/V_s in focused patches on the coasts of mainland Greece and northern Peloponnese at 7-11 km depth, which are associated with earthquake clusters and point towards fluid activity (Latorre et al., 2004). High intrinsic attenuation in all frequency bands confirms the major role played by fluid movement in the tectonics of this area. The complex style of deformation caused by shallow faults rooting from a north-dipping seismic zone and extensive fractures generated by fluid movement are potential sources of high scattering attenuation. The structures causing scattering and intrinsic anomalies can be of varying size from few kilometers to few hundred meters across as the attenuation anomalies are seen in all frequency bands. Towards the south-east of

the Gulf of Corinth lies the volcanic group of Methana-Sousaki, which exhibits high intrinsic attenuation in 1-2 and 2-4 Hz band. These sites are well known for their hydrothermal activity and exhibit a continuous release of methane (D'Alessandro et al., 2011), which may be the likely cause of the observed high intrinsic attenuation.

In the Santorini-Amorgos tectonic zone, our results show high Q_i^{-1} in 1-2 Hz, slightly high Q_i^{-1} in 2-4 Hz and high Q_{sc}^{-1} up to 8-16 Hz band. In addition, scattering attenuation is dominant over intrinsic attenuation in all frequency bands. These results are consistent with the findings of Ventouzi et al. (2018) who estimated high average S-wave attenuation at crustal depths in Cyclades using the acceleration spectra of intermediate depth earthquakes. In 1-2 Hz band of our results, the spread of a high anomaly across Cyclades indicates a possible link with the metamorphic core complexes (MCCs). The islands of the Cyclades including the ones in this zone contain outcrops of HT and HP MCCs, which are crustal blocks metamorphosed at deeper depths and emplaced back to the surface along extensional detachments (Tirel et al., 2013). The HT and HP conditions at the location of MCCs under exhumation can explain the high intrinsic attenuation. Considering a central frequency of 1.5 Hz and average crustal velocity of 3.3-3.6 km/s, the size of MCCs below the surface can be more than a few kilometers across. High scattering attenuation up to 8-16 Hz band have NE-SW orientation, which is likely associated with the normal faults as well as the Kameni-Kolumbo fracture zone. This zone bounds the source region of 2011-12 Santorini unrest and controls the magmatism at three volcanic centers: Kolumbo, Santorini, and Christiana, also aligned in NE-SW direction (Heath et al., 2019). Anomalies also overlap several NE-SW oriented normal faults, one of which produced the Mw 7.6, 1956 Amorgos earthquake (Brüstle et al., 2014; Konstantinou, 2010). The distributed faulting from earthquakes along the normal faults as well as micro-fractures due to fluid movement would generate significant crustal inhomogeneities that possibly cause

high scattering attenuation. Santorini and Kolumbo volcanic regions show relatively high scattering attenuation compared to intrinsic attenuation (Figure 7), which is similar to other volcanoes around the world (e.g. Prudencio et al., 2017; Wegler, 2003). Estimates of S-wave scattering using peak delay times of intermediate depth earthquakes also show increased scattering strength with increasing frequency even at crustal depths (Ranjan et al., 2019). These observations indicate that the faults, fractures or inhomogeneities generated by fluid movement outweigh the effect of thermal gradients generated by the fluid itself on seismic attenuation. The size of these structures based on strong anomalies up to 8-16 Hz band can be in the range of few hundred meters to few kilometers. Absence of high intrinsic attenuation for the volcanic centers above 2-4 Hz (Figure 6) is similar to that observed in Japan for the volcanoes in the Tohoku region (Carcolé & Sato, 2010). A satisfactory explanation as to why this occurs has not been proposed yet.

We observe high Q_{sc}^{-1} for Crete as well as higher Q_{sc}^{-1} than Q_i^{-1} in all frequency bands, while moderately high Q_i^{-1} in 1-2 Hz and 4-8 Hz band. Geochronological studies of paleoshorelines in Crete indicate that materials removed from the Nubian crust underplate the lower Aegean crust and cause the uplift of Crete (Ott et al., 2019). Materials from the oceanic crust accreted below the lower continental crust may undergo deformation with metamorphism under high-pressure conditions (Tirel et al., 2008) and possibly produce scattering attenuation. The exhumed MCCs on the island suggest that serpentinized mantle material flowing updip in a subduction channel extrudes in the deeper crust of Crete (Meier et al., 2007). The metamorphosed material flowing updip from the subduction interface in the back-arc to the base of the Cretan crust might penetrate it in the form of intrusions. These structures create high thermal gradients and therefore are a potential source of the intrinsic attenuation observed in 1-2 Hz and 4-8 Hz band. Even if the MCCs on Crete have origins similar to the ones on

Cyclades, the HT and HP conditions during their evolution would cause high absorption of seismic energy (Tirel et al., 2013). Other paleoshoreline studies also show that large earthquakes occurred on subduction related thrust faults, splay faults (365 AD earthquake), or normal faults offshore south Crete episodically (Mouslopoulou et al., 2015). Large earthquakes generate fractures that provide pathways for fluid movement from the subduction interface to the surface. These fractures could be the source of high scattering up to 8-16 Hz in Crete. The dominance of scattering attenuation over intrinsic attenuation (Figure 7) suggests that these anomalies are not a direct consequence of fluid activity, instead faults generated by large earthquakes or underplated inhomogeneous material may play an important role. Moderately high intrinsic attenuation in 1-2 Hz and 4-8 Hz, in spite of scattering attenuation being dominant, indicates that the MCCs produce a major portion of these anomalies. Assuming an average crustal velocity of 3.3-3.6 km/s and central frequency of 1.5 Hz to 6 Hz, the expected size of these intrusions should be in the order of few kilometers. Structural features generated by large earthquakes or underplated oceanic material on the other hand, vary in size from few kilometers to few meters as evidenced by high scattering attenuation in all four frequency bands.

The Gulf of Gökova shows moderately high Q_{sc}^{-1} in intermediate frequency bands and high Q_{sc}^{-1} in 1-2 Hz and 8-16 Hz bands, while high Q_i^{-1} in 1-2 Hz and moderately high Q_i^{-1} in higher frequency bands. The Gulf of Gökova is an E-W trending graben located in the western Turkey (Figure 1). The regional stress field shows that WNW-ESE normal faulting is the dominant deformation mechanism in the Gökova basin (Kapetanidis & Kassaras, 2019; Konstantinou et al., 2017; Andinisari et al., 2019), which is confirmed by seismic surveys (Tur et al., 2015). Besides, a NE-SW zone of left-lateral strike slip motion also appears in seismic sections that centrally divides the gulf (Işcan et al., 2013). The average S-wave attenuation estimated from

the acceleration spectra of intermediate depth earthquakes is also high in this region (Ventouzi et al., 2018). The high seismicity along the WNW-ESE normal faults and the NE-SW strike-slip zone have deformed the upper crust in the Gökova basin, which may be the source of high scattering attenuation in 1-2 Hz and 8-16 Hz bands. We observe relatively higher intrinsic attenuation than scattering attenuation in this region in 8-16 Hz band, which suggests that fluids may be present. However, there are no studies about the deeper crustal structure in this region, which can confirm the presence of fluids. The Kos-Nisyros-Yali volcanic field, which borders the Gulf of Gökova in the west, shows high intrinsic attenuation in 1-2 Hz band and high scattering attenuation in 8-16 Hz band. This volcano group also shows higher scattering attenuation than intrinsic attenuation. Local earthquake tomography of the Kos-Yali-Nisyros field indicates high V_p/V_s anomalies at 5-15 km and 25-35 km depths, which coincide with the gas emission zones around Yali and the collapsed Late Pliocene caldera of Nisyros-Kos. High V_p/V_s anomalies also exist to the south and south-west of this region at crustal depths, which is linked to the upward migration of magma from deeper reservoirs (Papadimitriou et al., 2018). The fractures generated by past eruptions in this region (Nomikou & Papanikolaou, 2011) and the velocity contrasts with the basement created by the intruded magma may influence the scattering attenuation. The fluid movement from the subduction interface to the magma reservoirs of these volcanoes and subsequent upward migration of fluids may be the cause of high intrinsic attenuation.

8. Conclusions

We used 2D sensitivity kernels based on perturbation theory in order to map the intrinsic and scattering attenuation derived from shear wave envelopes in the southern Aegean. The shear wave envelopes were calculated using the waveforms of 104531 relocated crustal events (< 40 km) with $M_L \leq 3.5$ in four frequency bands: 1-2, 2-4, 4-8 and 8-16 Hz. The shear wave

envelopes of each source-station path were inverted for ray path Q_{sc}^{-1} and Q_i^{-1} using a two-stage grid search with linear least squares inversion. We provide a simple way to incorporate the effect of mantle energy leakage into the 3D isotropic solution of radiative transfer equation. The southern Aegean was divided into square bins ($0.20^\circ \times 0.20^\circ$) and the sensitivity kernels for each ray path were calculated by the application of perturbation theory to the isotropic solution of the radiative transfer equation in 2D. The bin Q^{-1} were inverted from the Q^{-1} of ray paths and their sensitivity kernels using the MCMC algorithm, which provides a more robust estimate of seismic attenuation than spatial averaging. In our results, we identified four main regions that show high intrinsic and scattering attenuation: the Gulf of Corinth, the Santorini-Amorgos zone, Crete, and the Gulf of Gökova. High scattering attenuation observed in the Gulf of Corinth, the Santorini-Amorgos zone and the Gulf of Gökova is likely associated with the shallow normal faults or fractures generated by fluid movement. On the other hand, high scattering attenuation in Crete may emerge from the interaction of seismic waves with the deformed oceanic material underplated below the crust as well as fractures generated by large thrust earthquakes. High intrinsic attenuation in the Corinth rift is likely a consequence of the interaction of seismic waves with crustal fluids. The intrinsic attenuation in the Santorini-Amorgos zone (more broadly Cyclades) and Crete are likely associated with the MCCs. Based on strong anomalies in the intermediate frequency bands, the size of the MCCs could be in the order of few kilometers beneath the surface. Our results also show high intrinsic attenuation in the Gulf of Gökova, however, further studies are needed to decode the origin of these anomalies. Active volcanic centers display higher scattering attenuation than intrinsic attenuation similar to other volcanoes around the world.

Acknowledgments

We thank Jesùs M. Ibáñez and one anonymous reviewer for insightful comments that helped improve the manuscript. We also thank Kori Fajar Hermawan for picking phase arrivals and locating initial hypocenters for part of the CYCNET data. This research was funded by Taiwan International Graduate Program (TIGP) scholarship (P. Ranjan) and Ministry of Science and Technology (MOST) grant 109-2116-M-008-010 (K. I. Konstantinou). The EGELADOS and CYCNET waveform data are freely available for download from GFZ, Potsdam, European Integrated Data Archive (EIDA) (<http://eida.gfz-potsdam.de/webdc3/>) under the network code Z3 and ZZ while the HUSN waveform data are freely available for download from the National Observatory of Athens, EIDA archives under the network code HUSN (<http://eida.gein.noa.gr/>). All the analyses starting from raw waveforms were performed using MATLAB, version R2020a (academic license for NCU) and the figures were generated using Generic Mapping Tools (GMT), version 6 (Wessel et al., 2019). The catalogue of events used in this study as well as results for the final Q_{sc}^{-1} , Q_i^{-1} , and B_o along with GMT scripts to map them are uploaded to zenodo.org with DOI: <https://doi.org/10.5281/zenodo.4039552>.

References

- Aki, K., & Chouet, B. (1975). Origin of coda waves: Source, attenuation, and scattering effects. *Journal of Geophysical Research (1896-1977)*, 80(23), 3322–3342. <https://doi.org/10.1029/JB080i023p03322>
- Akinci, A., Pezzo, E. Del, & Malagnini, L. (2020). Intrinsic and scattering seismic wave attenuation in the Central Apennines (Italy). *Physics of the Earth and Planetary Interiors*, 303, 106498. <https://doi.org/https://doi.org/10.1016/j.pepi.2020.106498>
- Amante, C., & Eakins, B. E. (2009). Arc-Minute Global Relief Model: Procedures. *Data Source and Analysis, National Oceanic and Atmospheric Administration NOAA*.
- Andinisari, R., Konstantinou, K. I., & Ranjan, P. (2019). Seismotectonics of SE Aegean inferred from precise relative locations of shallow crustal earthquakes. *Journal of Seismology*. <https://doi.org/10.1007/s10950-019-09881-8>
- Argus, D. F., Gordon, R. G., & DeMets, C. (2011). Geologically current motion of 56 plates relative to the no-net-rotation reference frame. *Geochemistry, Geophysics, Geosystems*, 12(11), n/a-n/a. <https://doi.org/10.1029/2011GCO03751>
- Avallone, A., Briole, P., Agatza-Balodimou, A. M., Billiris, H., Charade, O., Mitsakaki, C., et al. (2004). Analysis of eleven years of deformation measured by GPS in the Corinth Rift Laboratory area. *Comptes Rendus - Geoscience*, 336(4–5), 301–311. <https://doi.org/10.1016/j.crte.2003.12.007>

Badi, G., Del Pezzo, E., Ibanez, J. M., Bianco, F., Sabbione, N., & Araujo, M. (2009). Depth dependent seismic scattering attenuation in the Nuevo Cuyo region (southern central Andes). *Geophysical Research Letters*, *36*(24). <https://doi.org/10.1029/2009GL041081>

Beckers, A., Hubert-Ferrari, A., Beck, C., Bodeux, S., Tripsanas, E., Sakellariou, D., & De Batist, M. (2015). Active faulting at the western tip of the Gulf of Corinth, Greece, from high-resolution seismic data. *Marine Geology*, *360*, 55–69. <https://doi.org/10.1016/j.margeo.2014.12.003>

Boschi, E., Giardini, D., & Morelli, A. (1991). MedNet: the very broad-band seismic network for the Mediterranean. *Il Nuovo Cimento C*, *14*(1), 79–99. <https://doi.org/10.1007/BF02509260>

Brüstle, A., Friederich, W., Meier, T., & Gross, C. (2014). Focal mechanism and depth of the 1956 Amorgos twin earthquakes from waveform matching of analogue seismograms. *Solid Earth*, *5*(2), 1027–1044. <https://doi.org/10.5194/se-5-1027-2014>

Brüstle, A., Kueperkoch, L., Rische, M., Meier, T., Friederich, W., & Group, E. W. (2012). Seismicity of the eastern Hellenic Subduction Zone. In *EGU General Assembly Conference Abstracts* (Vol. 14, p. 10426).

Burchfiel, B. C., Royden, L. H., Papanikolaou, D., & Pearce, F. D. (2018). Crustal development within a retreating subduction system: The Hellenides. *Geosphere*, *14*(3), 1119–1130. <https://doi.org/10.1130/GES01573.1>

Calvet, M., & Margerin, L. (2013). Lapse-Time Dependence of Coda Q: Anisotropic Multiple-Scattering Models and Application to the Pyrenees. *Bulletin of the Seismological Society of America*, *103*(3), 1993–2010. <https://doi.org/10.1785/0120120239>

Calvet, M., Sylvander, M., Margerin, L., & Villaseñor, A. (2013). Spatial variations of seismic attenuation and heterogeneity in the Pyrenees: Coda Q and peak delay time analysis. *Tectonophysics*, *608*, 428–439. <https://doi.org/https://doi.org/10.1016/j.tecto.2013.08.045>

Caputo, R., Catalano, S., Monaco, C., Romagnoli, G., Tortorici, G., & Tortorici, L. (2010). Active faulting on the island of Crete (Greece). *Geophysical Journal International*, *183*(1), 111–126. <https://doi.org/10.1111/j.1365-246X.2010.04749.x>

Caputo, R., Chatzipetros, A., Pavlides, S., & Sboras, S. (2013). The Greek Database of Seismogenic Sources (GreDaSS): state-of-the-art for northern Greece. *Annals of Geophysics*, *55*(5). <https://doi.org/10.4401/ag-5168>

Carcolé, E., & Sato, H. (2010). Spatial distribution of scattering loss and intrinsic absorption of short-period S waves in the lithosphere of Japan on the basis of the Multiple Lapse Time Window Analysis of Hi-net data. *Geophysical Journal International*, *180*(1), 268–290. <https://doi.org/10.1111/j.1365-246X.2009.04394.x>

Chib, S., & Greenberg, E. (1995). Understanding the Metropolis-Hastings Algorithm. *The American Statistician*, *49*(4), 327–335. <https://doi.org/10.1080/00031305.1995.10476177>

D'Alessandro, W., Brusca, L., Kyriakopoulos, K., Martelli, M., Michas, G., Papadakis, G., & Salerno, F. (2011). Diffuse hydrothermal methane output and evidence of methanotrophic activity within the soils at Sousaki (Greece). *Geofluids*, *11*(1), 97–107. <https://doi.org/10.1111/j.1468-8123.2010.00322.x>

De Siena, L., Amoruso, A., Pezzo, E. Del, Wakeford, Z., Castellano, M., & Crescentini, L. (2017). Space-weighted seismic attenuation mapping of the aseismic source of Campi Flegrei 1983–1984 unrest. *Geophysical Research Letters*, *44*(4), 1740–1748. <https://doi.org/10.1002/2017GL072507>

Del Pezzo, E., Ibañez, J., Prudencio, J., Bianco, F., & De Siena, L. (2016). Absorption and scattering 2-D volcano images from numerically calculated space-weighting functions. *Geophysical Journal International*, *206*(2), 742–756. <https://doi.org/10.1093/gji/ggw171>

Del Pezzo, E., Giampiccolo, E., Tuvé, T., Di Grazia, G., Gresta, S., & Ibañez, J. M. (2019). Study of the regional pattern of intrinsic and scattering seismic attenuation in Eastern Sicily (Italy) from local earthquakes. *Geophysical Journal International*, *218*(2), 1456–1468. <https://doi.org/10.1093/gji/ggz208>

Emoto, K., Sato, H., & Nishimura, T. (2010). Synthesis of vector wave envelopes on the free surface of a random medium for the vertical incidence of a plane wavelet based on the Markov approximation. *Journal of Geophysical Research: Solid Earth*, 115(8), B08306. <https://doi.org/10.1029/2009JB006955>

Eulenfeld, T., & Wegler, U. (2016). Measurement of intrinsic and scattering attenuation of shear waves in two sedimentary basins and comparison to crystalline sites in Germany. *Geophysical Journal International*, 205(2), 744–757. <https://doi.org/10.1093/gji/ggw035>

Fehler, M., Hoshiya, M., Sato, H., & Obara, K. (1992). Separation of scattering and intrinsic attenuation for the Kanto-Tokai region, Japan, using measurements of *S*-wave energy versus hypocentral distance. *Geophysical Journal International*, 108(3), 787–800. <https://doi.org/10.1111/j.1365-246X.1992.tb03470.x>

Friederich, W., & Meier, T. (2005). Egelados project 2005/07, RUB Bochum, Germany. Deutsches GeoForschungsZentrum GFZ. <https://doi.org/10.14470/M87550267382>

Gaebler, P., Eken, T., Bektaş, H. Ö., Eulenfeld, T., Wegler, U., & Taymaz, T. (2019). Imaging of shear wave attenuation along the central part of the North Anatolian Fault Zone, Turkey. *Journal of Seismology*, 23(4), 913–927. <https://doi.org/10.1007/s10950-019-09842-1>

Giannopoulos, D., Rivet, D., Sokos, E., Deschamps, A., Mordret, A., Lyon-Caen, H., et al. (2017). Ambient noise tomography of the western Corinth Rift, Greece. *Geophysical Journal International*, 211(1), 284–299. <https://doi.org/10.1093/gji/ggx298>

Heath, B. A., Hooft, E. E. E., Toomey, D. R., Papazachos, C. B., Nomikou, P., Paulatto, M., et al. (2019). Tectonism and Its Relation to Magmatism Around Santorini Volcano From Upper Crustal P Wave Velocity. *Journal of Geophysical Research: Solid Earth*, 124(10), 10610–10629. <https://doi.org/10.1029/2019JB017699>

Hoshiya, M. (1993). Separation of scattering attenuation and intrinsic absorption in Japan using the multiple lapse time window analysis of full seismogram envelope. *Journal of Geophysical Research*, 98(B9). <https://doi.org/10.1029/93jb00347>

Ibáñez, J. M., Castro-Melgar, I., Cocina, O., Zuccarello, L., Branca, S., Del Pezzo, E., & Prudencio, J. (2019). First 2-D intrinsic and scattering attenuation images of Mt Etna volcano and surrounding region from active seismic data. *Geophysical Journal International*, 220(1), 267–277. <https://doi.org/10.1093/gji/ggz450>

Ibáñez, J. M., Del Pezzo, E., De Miguel, F., Herraiz, M., Alguacil, G., & Morales, J. (1990). Depth-dependent seismic attenuation in the Granada zone (Southern Spain). *Bulletin of the Seismological Society of America*, 80(5), 1232–1244.

Işcan, Y., Tur, H., & Gökaşan, E. (2013). Morphologic and seismic features of the Gulf of Gökova, SW Anatolia: Evidence of strike-slip faulting with compression in the Aegean extensional regime. *Geo-Marine Letters*, 33(1), 31–48. <https://doi.org/10.1007/s00367-012-0307-x>

Kapetanidis, V., Deschamps, A., Papadimitriou, P., Matrullo, E., Karakonstantis, A., Bozionelos, G., et al. (2015). The 2013 earthquake swarm in Helike, Greece: seismic activity at the root of old normal faults. *Geophysical Journal International*, 202(3), 2044–2073. <https://doi.org/10.1093/gji/ggv249>

Kapetanidis, V., & Kassaras, I. (2019). Contemporary crustal stress of the Greek region deduced from earthquake focal mechanisms. *Journal of Geodynamics*, 123. <https://doi.org/10.1016/j.jog.2018.11.004>

Kokinou, E., Papadimitriou, E., Karakostas, V., Kamberis, E., & Vallianatos, F. (2006). The Kefalonia Transform Zone (offshore Western Greece) with special emphasis to its prolongation towards the Ionian Abyssal Plain. *Marine Geophysical Research*, 27(4), 241–252. <https://doi.org/10.1007/s11001-006-9005-2>

Konstantinou, K. I. (2010). Crustal rheology of the Santorini–Amorgos zone: Implications for the nucleation depth and rupture extent of the 9 July 1956 Amorgos earthquake, southern Aegean. *Journal of Geodynamics*, 50(5), 400–409. <https://doi.org/10.1016/J.JOG.2010.05.002>

Konstantinou, K. I., Evangelidis, C. P., Liang, W. T., Melis, N. S., & Kalogeras, I. (2013). Seismicity, *V_p/V_s* and shear wave anisotropy variations during the 2011 unrest at Santorini caldera, southern Aegean. *Journal of*

Volcanology and Geothermal Research, 267, 57–67. <https://doi.org/10.1016/j.jvolgeores.2013.10.001>

Konstantinou, K. I., Mouslopoulou, V., Liang, W.-T., Heidbach, O., Oncken, O., & Suppe, J. (2017). Present-day crustal stress field in Greece inferred from regional-scale damped inversion of earthquake focal mechanisms. *Journal of Geophysical Research: Solid Earth*, 122(1), 506–523. <https://doi.org/10.1002/2016JB013272>

Latorre, D., Virieux, J., Monfret, T., Monteiller, V., Vanorio, T., Got, J.-L., & Lyon-Caen, H. (2004). A new seismic tomography of Aigion area (Gulf of Corinth, Greece) from the 1991 data set. *Geophysical Journal International*, 159(3), 1013–1031. <https://doi.org/10.1111/j.1365-246X.2004.02412.x>

Lomax, A., Virieux, J., Volant, P., & Berge-Thierry, C. (2000). Probabilistic Earthquake Location in 3D and Layered Models (pp. 101–134). Springer, Dordrecht. https://doi.org/10.1007/978-94-015-9536-0_5

Margerin, L. (2017). Breakdown of equipartition in diffuse fields caused by energy leakage. *The European Physical Journal Special Topics*, 226(7), 1353–1370. <https://doi.org/10.1140/epjst/e2016-60165-6>

Margerin, L., Campillo, M., & Tiggelen, B. (1998). Radiative transfer and diffusion of waves in a layered medium: new insight into coda Q. *Geophysical Journal International*, 134(2), 596–612. <https://doi.org/10.1111/j.1365-246X.1998.tb07142.x>

Mayor, J., Calvet, M., Margerin, L., Vanderhaeghe, O., & Traversa, P. (2016). Crustal structure of the Alps as seen by attenuation tomography. *Earth and Planetary Science Letters*, 439, 71–80. <https://doi.org/https://doi.org/10.1016/j.epsl.2016.01.025>

Mayor, J., Margerin, L., & Calvet, M. (2014). Sensitivity of coda waves to spatial variations of absorption and scattering: radiative transfer theory and 2-D examples. *Geophysical Journal International*, 197(2), 1117–1137. <https://doi.org/10.1093/gji/ggu046>

Meier, T., Becker, D., Endrun, B., Rische, M., Bohnhoff, M., Stöckhert, B., & Harjes, H.-P. (2007). A model for the Hellenic subduction zone in the area of Crete based on seismological investigations. *Geological Society, London, Special Publications*, 291(1), 183–199. <https://doi.org/10.1144/SP291.9>

Meier, T., Bohnhoff, M., & Harjes, H.-P. (2004). Cyclades project 2002-2005 and Libyan Sea offshore project 2003-2004, RUB Bochum, Germany. Deutsches GeoForschungsZentrum GFZ. <https://doi.org/10.14470/MM7557265463>

Mesimeri, M., & Karakostas, V. (2018). Repeating earthquakes in western Corinth Gulf (Greece): implications for aseismic slip near locked faults. *Geophysical Journal International*, 215(1), 659–676. <https://doi.org/10.1093/gji/ggy301>

Mouslopoulou, V., Nicol, A., Begg, J., Oncken, O., & Moreno, M. (2015). Clusters of megathrust earthquakes on upper plate faults control the Eastern Mediterranean hazard. *Geophysical Research Letters*, 42(23), 10282–10289. <https://doi.org/10.1002/2015GL066371>

Napolitano, F., De Siena, L., Gervasi, A., Guerra, I., Scarpa, R., & La Rocca, M. (2020). Scattering and absorption imaging of a highly fractured fluid-filled seismogenic volume in a region of slow deformation. *Geoscience Frontiers*, 11(3), 989–998. <https://doi.org/https://doi.org/10.1016/j.gsf.2019.09.014>

Nomikou, P., & Papanikolaou, D. (2011). Extension of active fault zones on Nisyros volcano across the Yali-Nisyros Channel based on onshore and offshore data. *Marine Geophysical Research*, 32(1), 181–192. <https://doi.org/10.1007/s11001-011-9119-z>

Ott, R. F., Gallen, S. F., Wegmann, K. W., Biswas, R. H., Herman, F., & Willett, S. D. (2019). Pleistocene terrace formation, Quaternary rock uplift rates and geodynamics of the Hellenic Subduction Zone revealed from dating of paleoshorelines on Crete, Greece. *Earth and Planetary Science Letters*, 525, 115757. <https://doi.org/10.1016/j.epsl.2019.115757>

Paasschens, J. C. J. (1997). Solution of the time-dependent Boltzmann equation. *Physical Review E - Statistical Physics, Plasmas, Fluids, and Related Interdisciplinary Topics*, 56(1), 1135–1141. <https://doi.org/10.1103/PhysRevE.56.1135>

Pacchiani, F., & Lyon-Caen, H. (2010). Geometry and spatio-temporal evolution of the 2001 Agios Ioanis earthquake swarm (Corinth Rift, Greece). *Geophysical Journal International*, 180(1), 59–72. <https://doi.org/10.1111/j.1365-246X.2009.04409.x>

- Papadimitriou, P., Karakonstantis, A., Kapetanidis, V., Bozionelos, G., Kaviris, G., & Voulgaris, N. (2018). Seismicity and Tomographic Imaging of the Broader Nisyros Region (Greece) BT - Nisyros Volcano: The Kos - Yali - Nisyros Volcanic Field. In V. J. Dietrich & E. Lagios (Eds.) (pp. 245–271). Cham: Springer International Publishing. https://doi.org/10.1007/978-3-319-55460-0_8
- Papazachos, B. C., Karakostas, V. G., Papazachos, C. B., & Scordilis, E. M. (2000). The geometry of the Wadati-Benioff zone and lithospheric kinematics in the Hellenic arc. *Tectonophysics*, 319(4), 275–300. [https://doi.org/10.1016/S0040-1951\(99\)00299-1](https://doi.org/10.1016/S0040-1951(99)00299-1)
- Prudencio, J., Del Pezzo, E., Garcia-Yeguas, A., & Ibanez, J. M. (2013). Spatial distribution of intrinsic and scattering seismic attenuation in active volcanic islands - I: model and the case of Tenerife Island. *Geophysical Journal International*, 195(3), 1942–1956. <https://doi.org/10.1093/gji/ggt361>
- Prudencio, J., Manga, M., & Taira, T. (2018). Subsurface Structure of Long Valley Caldera Imaged With Seismic Scattering and Intrinsic Attenuation. *Journal of Geophysical Research: Solid Earth*, 123(7), 5987–5999. <https://doi.org/10.1029/2017JB014986>
- Prudencio, J., Taira, T., Aoki, Y., Aoyama, H., & Onizawa, S. (2017). Intrinsic and scattering attenuation images of Usu volcano, Japan. *Bulletin of Volcanology*, 79(4), 1–12. <https://doi.org/10.1007/s00445-017-1117-9>
- Ranjan, P., Konstantinou, K. I., & Andinisari, R. (2019). Spatial Distribution of Random Velocity Inhomogeneities in the Southern Aegean From Inversion of S Wave Peak Delay Times. *Journal of Geophysical Research: Solid Earth*, 124(10), 10393–10412. <https://doi.org/10.1029/2018JB017198>
- Reilinger, R., McClusky, S., Vernant, P., Lawrence, S., Ergintav, S., Cakmak, R., et al. (2006). GPS constraints on continental deformation in the Africa-Arabia-Eurasia continental collision zone and implications for the dynamics of plate interactions. *Journal of Geophysical Research: Solid Earth*, 111(B5), n/a-n/a. <https://doi.org/10.1029/2005JB004051>
- Ruscic, M., Bocchini, G. M., Becker, D., Meier, T., & van Keken, P. E. (2019). Variable spatio-temporal clustering of microseismicity in the Hellenic Subduction Zone as possible indicator for fluid migration. *Lithos*, 346–347. <https://doi.org/10.1016/j.lithos.2019.105154>
- Sato, H., Fehler, M. C., & Maeda, T. (2012). *Seismic wave propagation and scattering in the heterogeneous earth*. Springer Berlin Heidelberg. https://doi.org/10.1007/978-3-642-23029-5_5
- Shaw, B., Ambraseys, N. N., England, P. C., Floyd, M. A., Gorman, G. J., Higham, T. F. G., et al. (2008). Eastern Mediterranean tectonics and tsunami hazard inferred from the AD 365 earthquake. *Nature Geoscience*, 1(4), 268–276. <https://doi.org/10.1038/ngeo151>
- Shaw, B., & Jackson, J. (2010). Earthquake mechanisms and active tectonics of the Hellenic subduction zone. *Geophysical Journal International*, 181(2), 966–984. <https://doi.org/10.1111/j.1365-246X.2010.04551.x>
- Sodoudi, F., Kind, R., Hatzfeld, D., Priestley, K., Hanka, W., Wylegalla, K., et al. (2006). Lithospheric structure of the Aegean obtained from P and S receiver functions. *Journal of Geophysical Research: Solid Earth*, 111(B12), n/a-n/a. <https://doi.org/10.1029/2005JB003932>
- Takahashi, T., Sato, H., Nishimura, T., & Obara, K. (2007). Strong inhomogeneity beneath Quaternary volcanoes revealed from the peak delay analysis of S-wave seismograms of microearthquakes in northeastern Japan. *Geophysical Journal International*, 168(1), 90–99. <https://doi.org/10.1111/j.1365-246X.2006.03197.x>
- Tirel, C., Brun, J.-P., & Burov, E. (2008). Dynamics and structural development of metamorphic core complexes. *Journal of Geophysical Research*, 113(B4), B04403. <https://doi.org/10.1029/2005JB003694>
- Tirel, C., Brun, J. P., Burov, E., Wortel, M. J. R., & Lebedev, S. (2013). A plate tectonics oddity: Caterpillar-walk exhumation of subducted continental crust. *Geology*, 41(5), 555–558. <https://doi.org/10.1130/G33862.1>
- Tur, H., Yaltirak, C., Elitez, I., & Sarikavak, K. T. (2015). Pliocene-Quaternary tectonic evolution of the Gulf of Gökova, southwest Turkey. *Tectonophysics*, 638(1), 158–176. <https://doi.org/10.1016/j.tecto.2014.11.008>

Ventouzi, C., Papazachos, C., Hatzidimitriou, P., & Papaioannou, C. (2018). Anelastic P- and S- upper mantle attenuation tomography of the southern Aegean Sea subduction area (Hellenic Arc) using intermediate-depth earthquake data. *Geophysical Journal International*, 215(1), 635–658. <https://doi.org/10.1093/gji/ggy292>

Wegler, U. (2003). Analysis of multiple scattering at Vesuvius volcano, Italy, using data of the TomoVes active seismic experiment. *Journal of Volcanology and Geothermal Research*, 128(1–3), 45–63. [https://doi.org/10.1016/S0377-0273\(03\)00246-4](https://doi.org/10.1016/S0377-0273(03)00246-4)

Wessel, P., Luis, J. F., Uieda, L., Scharroo, R., Wobbe, F., Smith, W. H. F., & Tian, D. (2019). The Generic Mapping Tools Version 6. *Geochemistry, Geophysics, Geosystems*, 20(11), 5556–5564. <https://doi.org/10.1029/2019GC008515>

Accepted Article

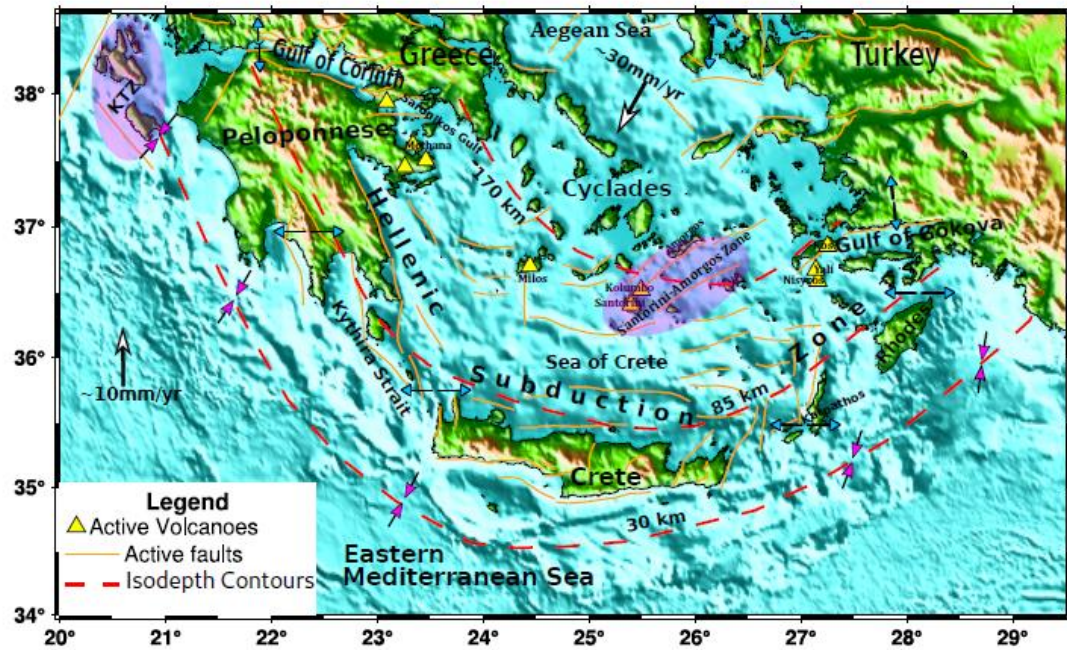


Figure 1: Map showing topographic and bathymetric features (from Etopo1: Amante et al., 2009) in the southern Aegean along with active faults (from GreDaSS: Caputo et al., 2013), Benioff zone isodepth contours (Pazpapachos et al., 2000) and active volcanoes (see Legend on the bottom left). The GPS velocities of the Aegean Sea plate and Nubian plate are marked with black arrows having white arrowheads (Argus et al., 2011). The regional stress field is shown using black arrows with blue and pink arrowheads.

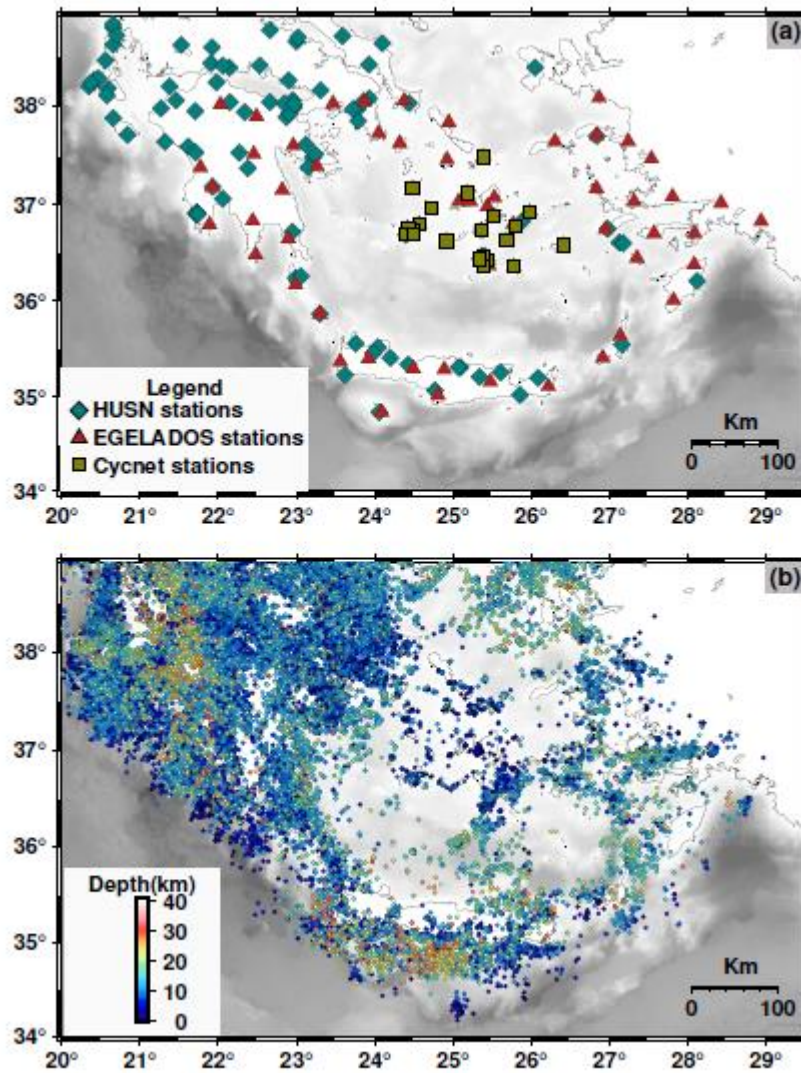


Figure 2: Maps showing (a) stations from temporary and permanent seismic networks in the southern Aegean and (b) epicenters of the crustal events (< 40 km deep) used in this study color coded according to hypocentral depth.

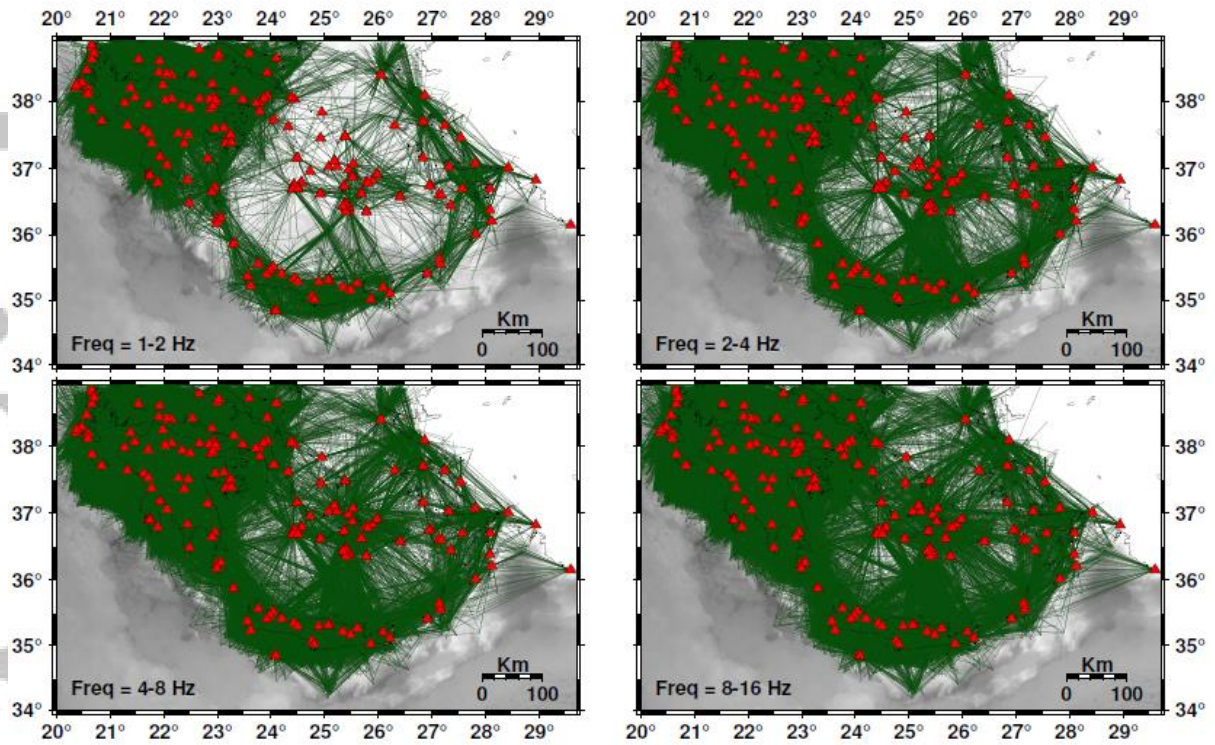


Figure 3: Maps showing ray paths (green) from source to stations (red triangles) in different frequency bands used in this study.

Accepted

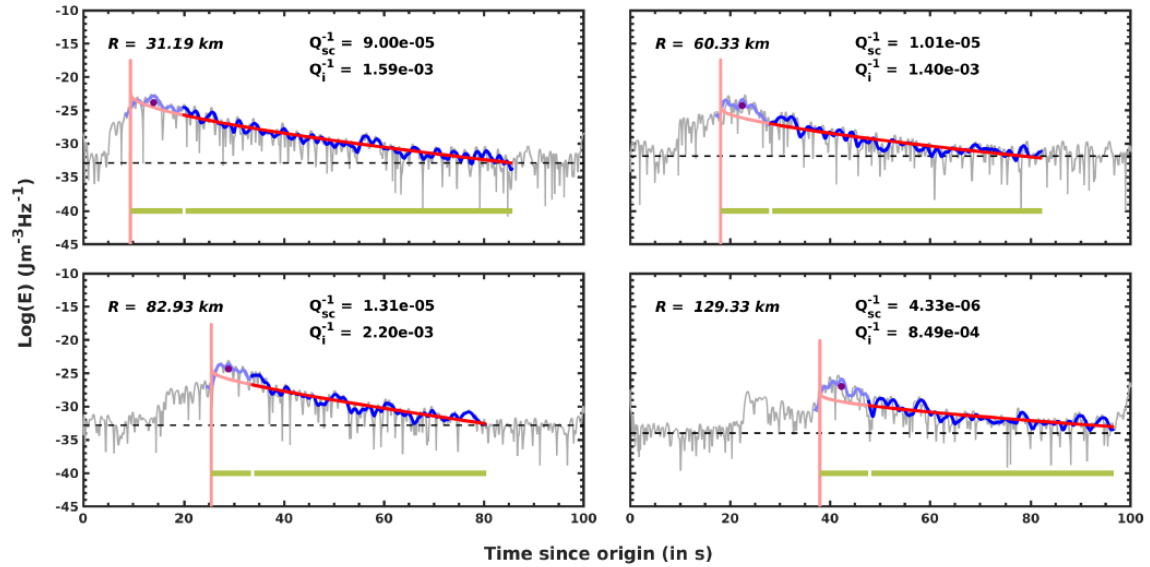


Figure 4: An example showing the fitting of the observed and calculated S-wave envelopes in 4-8 Hz frequency band from an event in central Peloponnese (origin time: 2010-01-03T22:46:56 UTC, M_L 2.4, 8 km deep) for different hypocentral distances. The logarithm of the observed (grey), the smoothed (blue) and the modeled S-wave envelopes (red) are shown. The horizontal bars at the bottom indicate the length of early-S window and the S-coda window in each frequency band. The location of early-S window mean for both the observed and modeled S-envelopes is shown with a dot in each frequency band, as the means overlap in logarithmic scale. The noise level is shown with dotted black line. The maximum allowed lapse time is 100 s (time since the origin of the event).

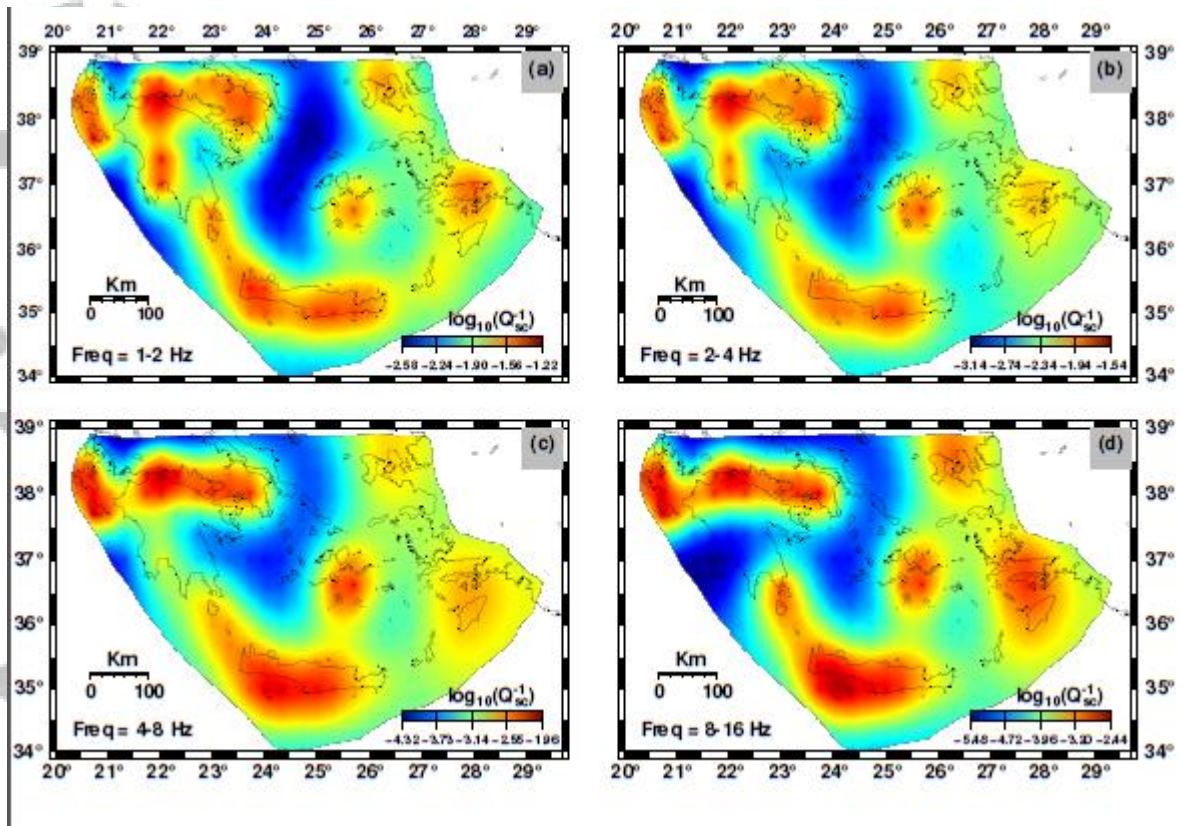


Figure 5: Spatial variation of $\log_{10}(Q_{sc}^{-1})$ in 1-2, 2-4, 4-8 and 8-16 Hz bands for the southern Aegean (see text for more details). Additional polygon mask closely following the outer limit of station distribution was applied at the end.

Accepted

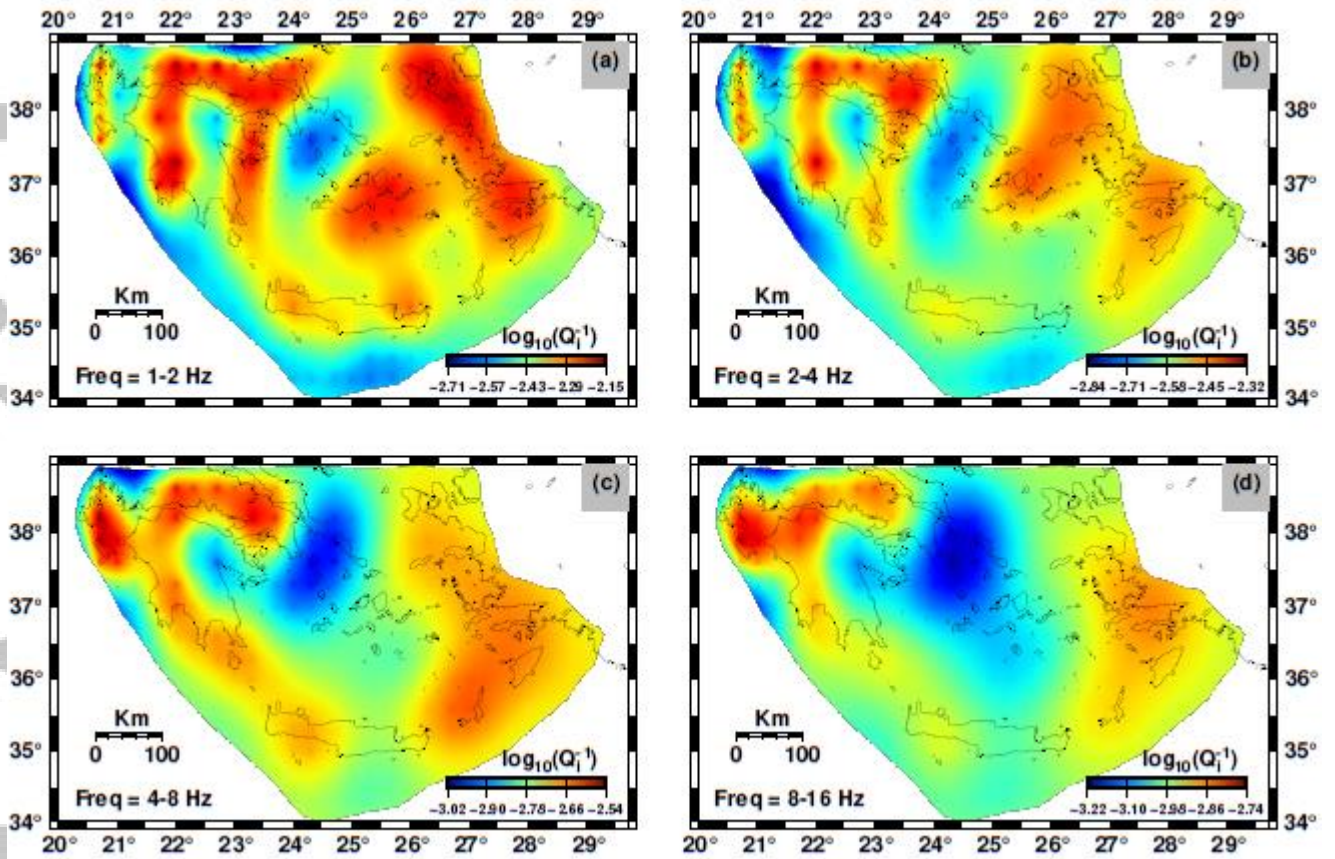


Figure 6: Spatial variation of $\log_{10}(Q_i^{-1})$ in 1-2, 2-4, 4-8 and 8-16 Hz bands for the southern Aegean (see text for more details). Same polygon mask is applied as in Figure 5.

Accepted

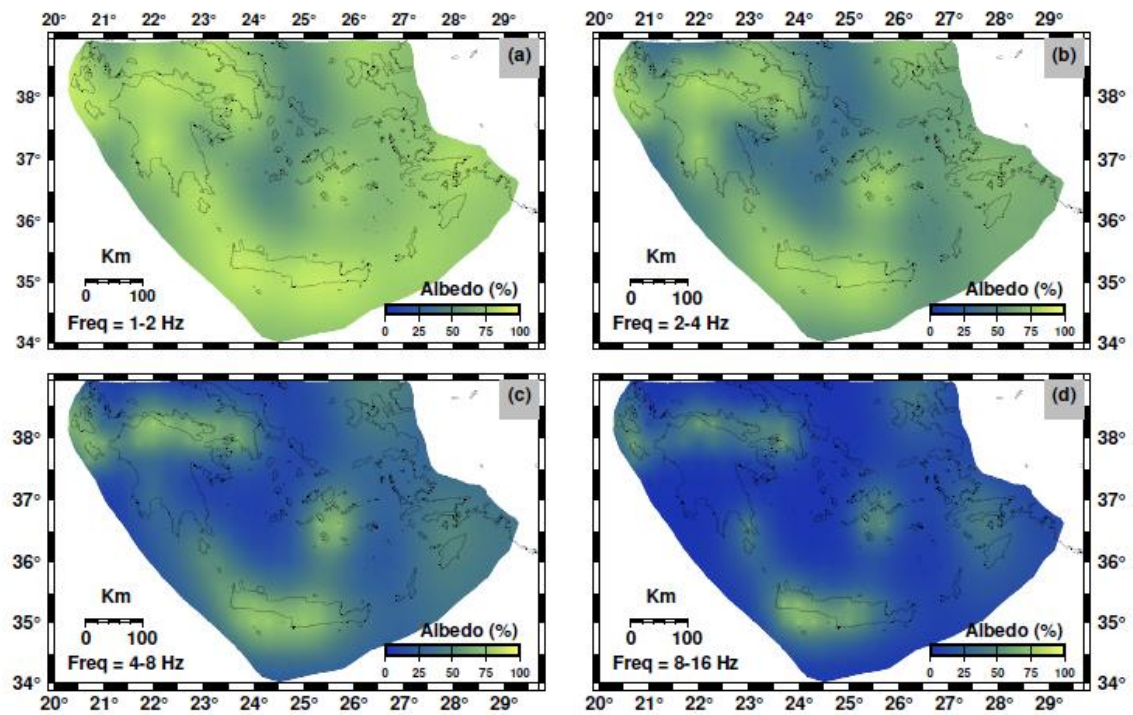


Figure 7: Spatial distribution of percentage strength of scattering attenuation versus total attenuation (seismic albedo) in 1-2, 2-4, 4-8 and 8-16 Hz bands (see text for more details). Same polygon mask is applied as in Figure 5.